



Atomic-scale structure and composition of Pt₃Co/C nanocrystallites during real PEMFC operation: A STEM–EELS study

Miguel Lopez-Haro^{a,b}, Laetitia Dubau^b, Laure Guétaz^c, Pascale Bayle-Guillemaud^a, Marian Chatenet^{b,e}, Johan André^d, Nicolas Caqué^d, Elisabeth Rossinot^d, Frédéric Maillard^{b,*}

^a CEA, INAC/UJF-Grenoble 1, UMR-E, SP2M, LEMMA, Minatec, 38054 Grenoble Cedex 9, France

^b Laboratoire d'Electrochimie et de Physico-chimie des Matériaux et des Interfaces, UMR 5279 CNRS/Grenoble-INP/Université de Savoie/Université Joseph Fourier, 1130 rue de la piscine, BP75, 38402 Saint Martin d'Hères Cedex, France

^c CEA, LITEN, Département des Technologies de l'Hydrogène, Laboratoire des Composants PEM, 17 rue des Martyrs, 38054 Grenoble, France

^d Axane, 2 rue de Clémence, BP 15, 38360 Sassenage, France

^e Member of the French University Institute (IUF)

ARTICLE INFO

Article history:

Received 23 November 2013

Received in revised form 15 January 2014

Accepted 20 January 2014

Available online 28 January 2014

Keywords:

Proton exchange membrane fuel cell

Oxygen reduction reaction

Pt–Co/C nanoparticles

Electrocatalyst degradation mechanisms

Atomic-scale spectroscopic imaging

ABSTRACT

The oxygen reduction reaction (ORR), which is the cathodic reaction in a proton-exchange membrane fuel cell (PEMFC) and in several other important processes, is a widely studied reaction. From the kinetics viewpoint, Pt is the best electrocatalyst and its activity can be increased upon alloying with a 3d-transition metal (Co, Ni, Fe, Cu). Aberration-corrected scanning transmission electron microscopy and electron energy loss spectroscopy prove that the structural and compositional changes of Pt₃Co/C nanoparticles during real-life PEMFC operation are much richer than previously thought from accelerated stress tests. Four different nanostructures are observed after 3422 h of operation in stationary mode: Pt, Pt–Co/C “hollow”, Pt–Co core–shell and Pt “bulk” nanoparticles. The presence of “hollow” nanoparticles in the aged catalytic layer is accounted for by the nanoscale Kirkendall effect, a vacancy-mediated diffusion mechanism in binary alloys where one species diffuses faster than the other. The oxygen reduction reaction specific activity of the “hollow” nanostructures is 1.5-fold that of the fresh Pt₃Co/C cathode catalyst and 3-fold that of Pt/C nanoparticles, thereby offering a new route to synthesize highly active and durable PEMFC electrocatalysts.

© 2014 Elsevier B.V. All rights reserved.

1. Introduction

Electrocatalysis plays a pivotal role in sustainable energy conversion and storage systems, such as water electrolyzers, metal–air batteries and low-temperature proton-exchange membrane fuel cells (PEMFCs). PEMFCs typically use bimetallic Pt–M alloys (with M = Co, Ni, Fe or Cu) at the cathode to enhance the rate of the oxygen reduction reaction (ORR) with respect to Pt [1–9]. On extended surfaces, the maximal enhancement in ORR catalytic activity is obtained for atomic composition of 3:1 (Pt:M), but the catalytic efficiency of the surface may be further improved by using segregated single Pt surface layer (called Pt “skin” surface), and controlling the fine distribution of M atoms in the near surface layers [3,7]. Stamenkovic et al. [4] showed that a Pt₃Ni(1 1 1) surface is intrinsically 10-fold more active for the ORR than a Pt(1 1 1) and 90-fold than a state-of-the-art Pt/C. This extraordinary performance arises

from compositional oscillations between the outermost and third layers, which are Pt-rich, and the second atomic layer, which is Ni-rich. Unfortunately, Pt-based cathode catalyst materials are neither able to maintain their favourable structural arrangement, nor consequently their superior catalytic performance over pure Pt/C on the long term [1,8,10–14]. In an early study, Watanabe et al. [1] noticed that surface and “bulk” Co atoms, that is Co atoms located in the interior of the Pt₃Co/C nanoparticles, are dissolved following a chronoamperometry step in phosphoric acid at 0.80 V vs. the reversible hydrogen electrode (RHE). Later, Zignani et al. [15] and Colon-Mercado et al. [11] reported dissolution of both Pt and Co atoms from Pt₃Co/C nanoparticles and redeposition of Pt²⁺ ions (z = 2, 4) on top of other particles during accelerated stress tests (ASTs) based on potentiodynamic potential modulation. Both phenomena yield the formation of a thick Pt-enriched shell covering the Co-depleted mother core as confirmed by anomalous small angle X-ray scattering, [16] Synchrotron X-ray diffraction, [17] electron microscopy [13,18] and electron energy loss spectroscopy (EELS), [19–21] which decreases the strain and ligand effect of the non-noble element [7].

* Corresponding author. Tel.: +33 476 826 588; fax: +33 476 826 777.
E-mail address: frederic.maillard@lepmi.grenoble-inp.fr (F. Maillard).

Most of the knowledge on the degradation mechanisms of Pt–M nanoalloys arises from ASTs. These tests allow unveiling the effect of stress parameters, such as temperature, relative humidity and electrode potential, and avoiding lengthy on-site PEMFC aging tests. However, they exert a strong impact on the final nanostructure of the Pt–M catalyst. For example, it has been shown that potential cycling between 0.60 and 1.00 V vs. RHE that is routinely performed to mimic load–cycling in a vehicle [22,23] causes the formation of Pt–Co core–Pt shell nanostructures following the dissolution and the redeposition of Pt atoms at the upper/lower potential limit, respectively [13,20]. Therefore, the value of the lower potential limit controls whether Pt^{2+} ions produced at the upper potential limit are electrochemically redeposited or not onto the remaining bimetallic nanoparticles [24]. In two recent studies, Yu, Xin and co-workers [20,25] compared the degradation of a $\text{Pt}_3\text{Co}/\text{C}$ catalyst aged in a PEMFC stack (solid polymer electrolyte) or in a liquid half-cell (liquid electrolyte). They reported an increase of the mean crystallite size in both cases, but larger extent of electrochemical Ostwald ripening in the AST performed in the fuel cell (that is thicker Pt-enriched shell) than in the liquid half-cell. Besides the very different ageing conditions in a controlled laboratory experiment or in a fuel cell stack (where the voltage, the temperature, the humidity, and the gas composition are prone to change rapidly), this result suggests that the solid electrolyte confines the Pt^{2+} ions produced by the electrochemical Ostwald ripening at close proximity of the bimetallic nanocrystallites, and thus promotes their redeposition. On the contrary, liquid electrolyte allows fast diffusion of Pt^{2+} ions in the bulk of the solution thus minimizing the extent of redeposition. It is also worth noting that different gaseous atmosphere are used during AST in an electrochemical cell (where an inert gas feeds the cathodic compartment [20,25]) or during PEMFC operation (where oxygen is fed to the cathode [12,14,26,27]), which also cause differences in the final nanostructure of the catalyst. In a recent study, Dubau et al. [28] reported, using identical location transmission electron microscopy, that reducing species (H_2 , CO, methanol) promote the migration/aggregation of Pt nanocrystallites supported on a high surface area carbon black whereas oxidizing species (O_2) accelerate the corrosion of the carbon support and the detachment of the Pt nanoparticles. A decreased contribution of electrochemical Ostwald ripening was observed in the presence of CO and O_2 with respect to Ar atmosphere. These results show that the same AST performed under neutral (N_2 , Ar) or oxidizing (O_2) atmosphere yields different degradation pathways, and thus different electrochemically active surface area (ECSA) losses. They also put into question the relevance of ASTs, usually performed in neutral atmosphere, to mimic the oxidizing PEMFC cathode operating conditions. Summing up, real-life PEMFC aging tests remain essential to the understanding of the compositional and structural modification of Pt-alloy nanoparticles on the long term.

In this study, we investigated at the atomic scale the structural and compositional modifications of commercial $\text{Pt}_3\text{Co}/\text{C}$ nanocatalysts during a 3422 h PEMFC aging test. Using aberration-corrected scanning transmission electron microscopy (STEM) and electron energy loss spectroscopy, X-ray energy dispersive spectroscopy (X-EDS) and electrochemical techniques, we provide a full picture of the different nanostructures formed from the mother $\text{Pt}_3\text{Co}/\text{C}$ nanoparticles, and bridge these changes to their intrinsic ORR activity.

2. Experimental

2.1. Materials

The anode (Pt/C) and the cathode ($\text{Pt}_3\text{Co}/\text{C}$) materials, the chemical nature of the ionomer contained in the catalytic layers and

the proton-exchange membrane are proprietary and will not be described. Two Pt/C electrocatalysts supported on Vulcan[®] XC-72 carbon black with a weight fraction of 20% or 40% were purchased from E-TeK and used as reference materials. These electrocatalysts possess surface averaged mean particle size of 2.9 and 4.5 nm, respectively, and were used as-received without any further treatment (more details can be found in Ref. [29]).

2.2. PEMFC testing

A 16-cell short PEMFC stack using Pt/C at the anode and $\text{Pt}_3\text{Co}/\text{C}$ at the cathode was operated at constant current ($I = 50$ A, translating into an average current density of $j = 0.60$ A cm⁻²) for $t = 3422$ h at $T = 343$ K. The catalytic layers were catalyst-coated membranes electrodes (geometric area 85 cm²). The cathode was fed with humidified air (65% relative humidity (RH), 1.1 bar abs., gas stoichiometry of 2.5), and the relative humidity was fixed at the gas inlet by an adequate choice of the humidifier and cell temperatures. The anode was fuelled with dry pure dihydrogen (0% RH, 1.3 bar abs., dead-end mode, corresponding to an average H_2 stoichiometry of ca. 1). The gas flow rates were 5.6 and 33.2 N L min⁻¹ for H_2 and air, respectively. Air and H_2 purges were performed intermittently to remove the water produced at the cathode and the water/nitrogen that accumulate at the anode, respectively. The stacks were disassembled after different life stages: some of the membrane electrode assemblies (MEAs) were removed and used for physical, chemical and electrochemical characterization (cell 10 after 1163 and 2259 h of operation and cell 8 after 3422 h of operation. These cells were located in the middle of the stack, thus ensuring reproducible and well-controlled aging conditions). All the data presented in this study were obtained for electrocatalysts sampled in the cathode inlet region of the MEA, which is the region of harshest degradation in the present operating conditions [27].

2.3. Electrochemical measurements

The electrochemical measurements performed with the fresh/aged catalytic materials were conducted using an Autolab PGSTAT20 in a custom-made four-electrode electrochemical cell thermostated at $T = 298$ K. Prior to any electrochemical measurement, the electrochemical cell and all glassware accessories were cleaned by soaking in a $\text{H}_2\text{SO}_4:\text{H}_2\text{O}_2$ mixture and thorough washing with ultrapure water. Fresh electrolyte solution (0.1 M H_2SO_4) was daily prepared with Milli-Q water (Millipore, 18.2 M Ω cm, total organic compounds <3 ppb) and H_2SO_4 96 wt% (Suprapur, Merck). The counter-electrode was a large-area Pt foil and the reference electrode – a mercury sulphate electrode (MSE) $\text{Hg}|\text{Hg}_2\text{SO}_4|\text{K}_2\text{SO}_4$ (saturated, aqueous) – connected to the cell via a Luggin capillary. However, all electrode potentials are given vs. reversible hydrogen electrode (RHE) scale ($E_{\text{MSE}} = 0.72$ V vs. RHE). A Pt wire connected to the reference electrode was used to filter the high frequency electrical noise and to avoid disturbing the low frequency electrical measurements. More details on the dual-reference system used in this work can be found in Ref. [30].

To prepare the working electrodes, an ink composed of 5 mg of the commercial Pt/C, acid-leached “hollow” Pt–Co/C or Pt–Co/C scraped from fresh/aged catalytic layers, 54 μL of 5 wt% Nafion[®] solution (Electrochem. Inc.) and 2.4 mL (18.2 M Ω cm) of deionized water (MQ-grade, Millipore) was prepared according to a home-made procedure described in Ref. [14]. After sonication for 15 min, 10 μL of the suspension was pipetted onto a glassy carbon disk (Sigradur[®] G, geometric surface area 0.196 cm²) and sintered for >5 min at $T = 383$ K to ensure evaporation of the Nafion[®] solvents yielding a loading of 30 $\mu\text{g}_{\text{Pt-Co/C}}$ or $\mu\text{g}_{\text{Pt/C}}$ cm⁻². Before the measurements, the working electrode was immersed into the electrolyte at 0.10 V vs. RHE under potential control. The

surface reactivity and the intrinsic ORR activity of the fresh and the aged catalytic materials were determined using cyclic or linear sweep voltammetry, respectively. In cyclic voltammetry, prior to any experiment, the solution was purged with argon (>99.999%, Messer) for 20 min, to remove any oxygen. A reliable estimation of the real surface area of Pt–Co/C with different Co content is possible using the CO_{ad} stripping coulometry [12] assuming that CO adsorbs on Pt atoms only and that the electrooxidation of a CO_{ads} monolayer requires $420 \mu\text{C cm}^{-2}$ of Pt. Carbon monoxide stripping experiments were carried out by first bubbling the solution with CO for 6 min and then with argon for 39 min, while the potential was held at +0.10 V vs. RHE. Two carbon monoxide stripping experiments were carried out before and after the electrocatalytic measurements to verify that no structural or chemical change occurred during the experiments: only slight variations (<2%) of the ECSA were monitored, and therefore the value determined before the ORR measurements was used. The intrinsic ORR activity was measured in O₂-saturated 0.1 M H₂SO₄ solution (20 min of purging by oxygen >99.99%, Messer) by linearly sweeping the potential from 0.40 to 1.05 V at a scan rate of 2 mV s^{-1} and at a revolution rate of 1600 rpm. The intrinsic ORR specific activity was determined at $E = 0.90 \text{ V}$ vs. RHE by normalizing the current measured after correction from the oxygen diffusion in the solution to the real surface area determined by CO_{ad} stripping voltammetry. Further details about the chemicals used, the preparation of the electrolytic solutions, and the experimental set-up can be found in Ref. [14].

2.4. Electron microscopy

The X-ray energy dispersive spectroscopy (X-EDS) spectra were performed on the Pt–Co/C powder scraped from the fresh/aged catalytic layers, and deposited on a copper grid bearing a lacey carbon membrane. The samples were examined with a LB FEI Titan 80–300 microscope operated at 200 kV and equipped with a Cs probe corrector. A condenser aperture of 50 μm and a 128 mm camera length was used, obtaining an electron probe with a convergence angle of 17 mrad. In order to get a high signal-to-noise ratio, a spot size 5 was used obtaining a beam current of 0.350 nA. The X-EDS spectra were recorded on individual nanoparticles by scanning the beam in a square region adjusted to the particle size using an acquisition time of 160 s. In the case of X-EDS line profile analyses, line-scans with image drift correction were carried out, recording a spectrum each 3 s. The quantitative analyses were performed on Pt L and Co K lines using the *K*-factor provide by the FEI TIA software.

The high-angle annular dark-field (HAADF) and the Spectrum-Imaging electron energy loss spectroscopy analyses were recorded on a FEI Titan³ Ultimate 80–300 microscope at CEA/PFNC Grenoble double Cs-corrected, and operating at 200 kV. The aberrations of the condenser lenses were corrected up to fourth-order using the Zemlin tableau to obtain a sub-Angstrom electron probe. A condenser aperture of 50 μm yielding an electron probe with a convergence angle of 20 mrad was used. The annular dark-field (ADF) collection angle ranged from 75 to 162 mrad and a 320 mm camera length on energy-filtered scanning transmission electron microscopy (EFSTEM) mode was used for EELS acquisitions, giving a collection semi-angle of 73 mrad. A Quantum–Gatan post column Imaging Filter (GIF) was used equipped with an ultra-fast shutter. To compensate for any sample drift during the analysis, a spatial drift correction was used every three line of the analysis. Every EEL spectrum was acquired using an acquisition time of 100 ms and an energy dispersion of 0.25 eV per channel. The matrix of spectra was de-noised using the standard principal component analysis and chemical maps were constructed analyzing the Pt N₃ (518 eV) and Co L_{2,3} (780 eV) edges using a power-law background subtraction. To estimate the effective shell thickness for the entire particle, the Co and Pt areas were found by counting all the pixels

that fell above a threshold (50% of the maximum signal intensity for each element). For the calculation of the Pt-shell thickness, we used the methodology recently developed by Xin et al. [20]. Briefly, the nanoparticle and the core were considered as spheres, and the difference between the Pt radius and Co radius was used as the shell thickness. Assuming a (1 1 1) lattice spacing of 0.220 nm for the fresh and the aged Pt–Co/C nanoparticles, a number of equivalent monolayers could be calculated. The Pt–Co/C catalyst models used in our high-resolution HAADF (HR-HAADF) image simulation studies were built with RHODIUS, a computer program developed at Cadiz University [31]. The TEMSIM software was used for HR-HAADF image simulations [32].

2.5. Synthesis of the “hollow” Pt/C nanoparticles

2.5.1. Chemicals

(Pt(NH₃)₄Cl₂ (Alfa Aesar, Specpure) and CoCl₂(6 H₂O) (Fluka, >98.0%) were reduced by NaBH₄ (Aldrich 99.99%). Ethanol was purchased from Sodipro. All the chemicals were used as received without further purification.

2.5.2. In-house synthesis of “hollow” Pt/C nanoparticles

Hollow Pt/C nanoparticles were synthesized by a one-pot, surfactant-free method derived from the study of Bae et al. [33]. First, 0.46 mmol of Pt(NH₃)₄Cl₂ and 0.46 mmol of CoCl₂ precursor solutions were mixed with 0.3 g Vulcan XC72® (Cabot), 10 mL of ethanol and 250 mL of de-ionized water (Millipore). An aqueous solution of NaBH₄ (5.5 mmol, 0.22 M) was then added at a rate of 5 mL min^{−1}, and stirred for 1 h under magnetic stirring. The resulting mixture was filtered, washed by de-ionized water (Millipore) several times and dried at 383 K during 45 min to yield “hollow” Pt_xCo_{1−x}/C nanoparticles. Acid-leaching of the Pt–Co/C nanoparticles was performed in 250 mL of 1 M H₂SO₄ with stirring under air for 24 h to remove Co/C nanoparticles that were not covered by Pt. The final electrocatalyst contain little Co (*ca.* 2–5 at%).

3. Results and discussion

Representative aberration-corrected high angle annular dark field scanning transmission electron microscopy (HAADF-STEM) images of the fresh and the 3422 h-aged Pt–Co/C nanoparticles are shown in Fig. 1. The pristine Pt₃Co/C nanoparticles feature {1 1 1} and {2 0 0} facets, in agreement with their predicted equilibrium structure (a truncated Wulff polyhedron). The metal particle size distribution (Fig. S1) ranges from 2 to 6 nm with a surface-averaged mean particle size of 5.2 nm. Such values are classical for commercial bimetallic electrocatalysts (see Refs [20,25,34,35]), in particular the rather sharp particle size distribution results from thermal treatments that are performed during the catalyst manufacturing to improve the resistance to electrochemical corrosion of the carbon support, prevent the detachment of the metal nanoparticles, and improve the cathode performance [36]. A high resolution HAADF-STEM image of an individual Pt₃Co/C nanoparticle is displayed in Fig. 1c: the random intensity variations observed between the atomic columns suggest that the alloyed Pt–Co face-centred cubic phase is disordered, in agreement with the results of previous studies on commercial bimetallic electrocatalysts [13,17,37].

Large morphological changes are noticed after 3422 h of operation at constant current (50 A, translating into an averaged current density of 0.6 A cm^{-2}). The aged Pt–Co/C nanoparticles possess a more spherical appearance (they are smoother, with smaller extent of low-coordination surface atoms), independently of their size (Fig. 1b). Substantial nanoparticle growth was found in the MEA cathode as revealed by 1.5 nm shift of the centre of the Pt–Co/C particle size histogram towards larger sizes (Fig. S1). Finally, the

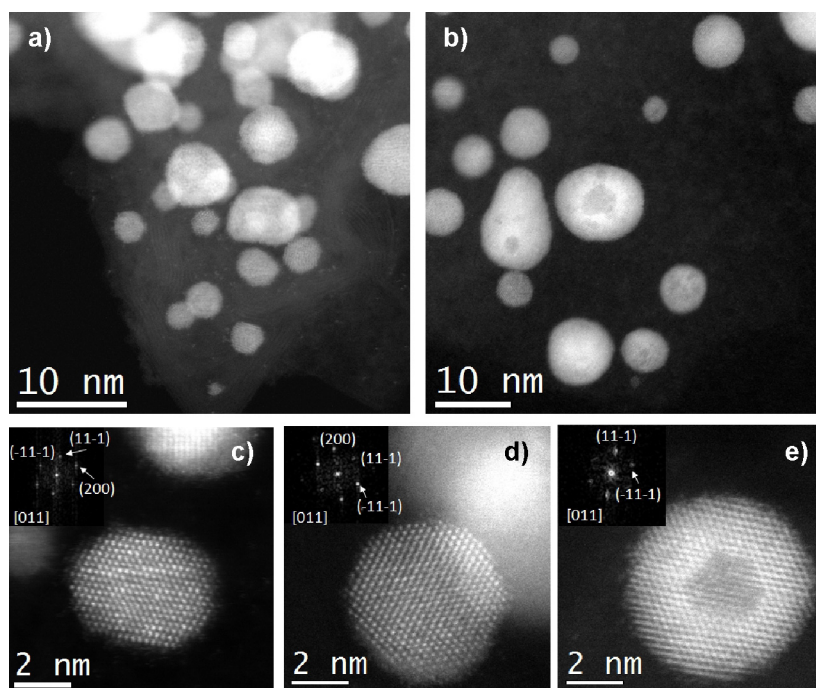


Fig. 1. Aberration-corrected HAADF-STEM images and digital diffraction pattern (DDP; insets) of the fresh and aged Pt-Co/C electrocatalysts. (a and c) as-received Pt₃Co/C nanoparticles, (b, d and e) Pt-Co/C nanoparticles after 3422 h of operation at $j = 0.6 \text{ A cm}^{-2}$ and $T = 343 \text{ K}$ showing the formation of “hollow” nanoparticles. Marked in DDPs are reflections characteristic of the cubic phase in the $[011]$ zone axis.

fraction of the smallest 2–3 nm-sized Pt-Co/C particles significantly decreased, at the benefit of aggregated Pt-Co/C with complex and irregular shapes. These results can be understood in view of the redeposition of Pt²⁺ ionic species coming from the dissolution of the smallest nanocrystallites onto larger ones (electrochemical Ostwald ripening) [13,20]. Not only does the morphology of

the nanoparticles change during PEMFC operation, but also their fine nanostructure and chemical composition. The aged Pt-Co/C nanoparticles appear homogeneous or feature dark-contrasted patches in HAADF-STEM images (see Fig. 1d and Fig. 1e, respectively). In this imaging mode, the contrast varies linearly with the mass and the thickness of the analysed area, and is proportional to

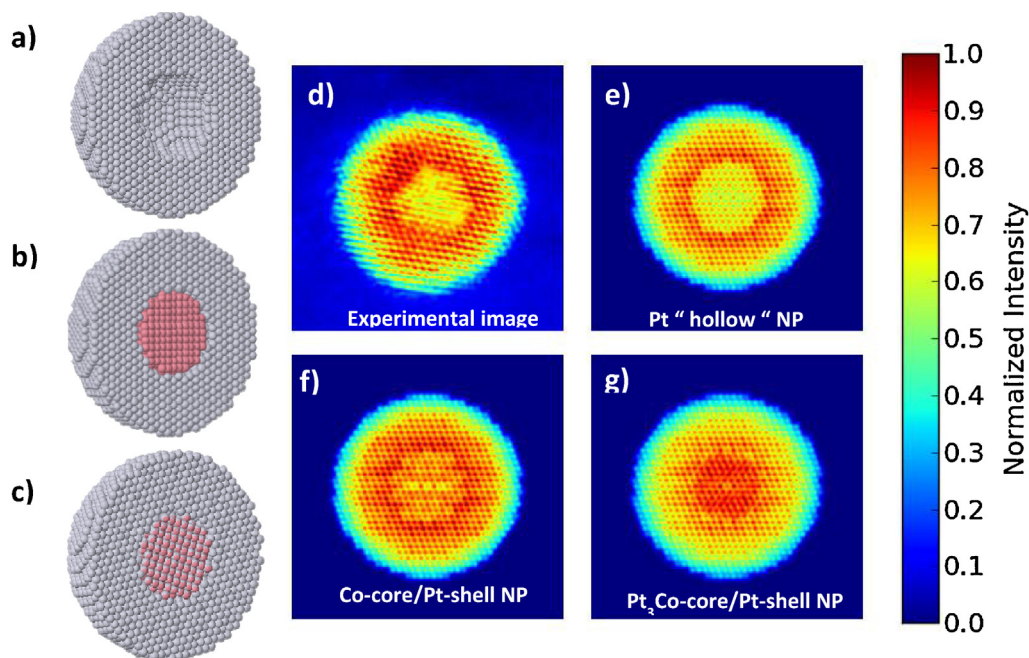


Fig. 2. Experimental and simulated images of nanoparticles featuring dark-contrasted patches in HAADF. Structural model of (a) a pure “hollow” Pt nanoparticle, (b) a Pt shell surrounding a pure Co core and (c) and Pt shell covering a Pt₃Co disordered alloy core. The experimental HAADF image is shown in (d) while the simulated HAADF images of the different models are displayed in (e–g). The following electron-optical parameters were used in accordance with the experiment: accelerating voltage = 200 kV, $C_3 = 0.001 \text{ mm}$, $C_5 = 5 \text{ mm}$, $\Delta f = -3 \text{ nm}$, convergence angle = 20 mrad and ADF collection angle = 75–162 mrad. The HAADF image simulations were convoluted with a 0.18 nm FWHM Gaussian. The images are displayed on a coloured scale to improve the visibility of the different intensity levels, and facilitate the correlation between experiment and simulations. (For interpretation of the references to color in this figure legend, the reader is referred to the web version of this article.)

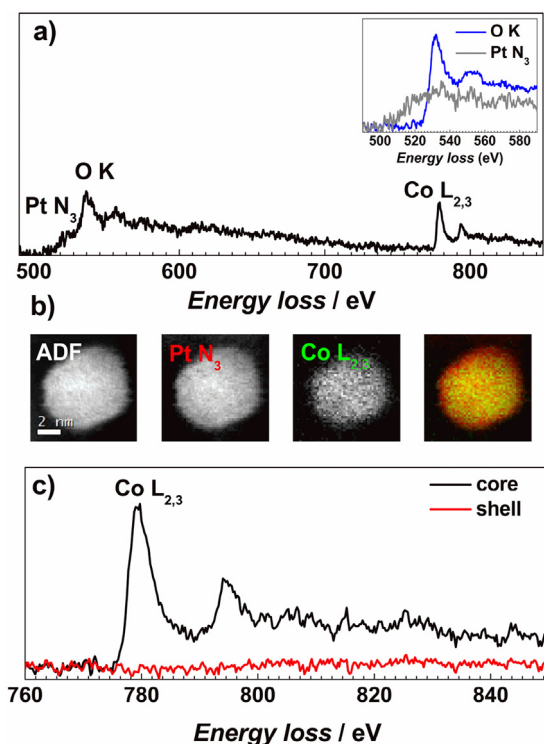


Fig. 3. (a) Representative EEL spectrum of a $\text{Pt}_3\text{Co/C}$ nanoparticle. The inset shows the Pt N_3 edge neighbouring the O K signal. Despite their overlap, both characteristic edges can clearly be distinguished. (b) ADF image and EELS-SI maps of an individual $\text{Pt}_3\text{Co/C}$ nanoparticle of the fresh catalyst obtained after de-noising the matrix of spectra using standard principal component analysis (Pt: red and Co: green). The scale bar is 2 nm. (c) EEL spectrum extracted from core and shell areas of the nanoparticle. These spectra indicate that the fresh nanoparticle presents a Co-free shell *ca.* 2 monolayer thick. (For interpretation of the references to color in this figure legend, the reader is referred to the web version of this article.)

the square of the mean atomic number Z of the specimen; therefore, the observed dark-contrast may come from either the presence of a cavity or a light element, *e.g.* Co ($Z=27$), in the core of the nanoparticle.

To get a better insight into the structure of the dark-contrasted nanoparticles, the normalized variations of the experimental HAADF intensity (Fig. 2d) were compared to simulations of HAADF images, using three different models: (i) a pure Pt nanoparticle containing a cavity in the centre (a “hollow” nanoparticle, Fig. 2e), (ii) a Pt shell surrounding a pure Co core (Fig. 2f) or (iii) a Pt shell covering a Pt_3Co disordered alloy core (Fig. 2g). Clearly, the best match is obtained with the “hollow” Pt nanoparticle model (Fig. 2e).

Additional insights into the chemical distribution of Pt and Co elements in the fresh and the aged Pt-Co/C nanoparticles were obtained from electron energy loss spectroscopy in spectrum-imaging mode (EELS-SI). In EELS-SI, the EEL spectrum and the high angle annular dark field signal are simultaneously collected at each point of the scan making it a unique technique to correlate chemical and structural information. A representative EEL spectrum obtained from the fresh $\text{Pt}_3\text{Co/C}$ electrocatalyst is presented in Fig. 3a: it features the characteristic signals for the Pt N_3 , O K and $\text{Co L}_{2,3}$ edges at 518, 532 and 780 eV, respectively. A matrix of EEL spectra was acquired by scanning the electron beam over a single nanoparticle. The signal was then de-noised using the standard principal component analysis (PCA), before calculating the chemical map for each element [20,38,39]. An ADF image and the corresponding chemical maps of a fresh $\text{Pt}_3\text{Co/C}$ nanoparticle are displayed in Fig. 3b. The coloured image presents the superimposition of Pt (red) and Co (green) atoms distributions, and provides

direct evidence of the formation of a Pt-enriched shell – *ca.* 3.4 monolayer-thick in average – with no detectable Co atom covering the mother Pt_3Co core (Fig. 3c), in agreement with previous observations on commercial $\text{Pt}_3\text{Co/C}$ nanoparticles [18,20]. Such nanostructure results from the “acid-leaching” procedure used at the industrial scale to remove surface or non-alloyed Co atoms from the pristine $\text{Pt}_3\text{Co/C}$ catalyst.

A detailed picture of the changes in structure and composition of the bimetallic nanoparticles after real PEMFC operation is shown in Fig. 4. Four different nanostructures are found in the aged catalytic layer: (i) Pt-Co/C core-shell nanoparticles characterized by an alloyed core surrounded by a thickened Pt-rich shell, (ii) Pt-Co/C “hollow” nanoparticles and (iii) pure Pt/C “hollow” nanoparticles, from which Co dissolution has been completed. The presence of “bulk” Pt/C nanoparticles (*i.e.* containing no cavity) was also evidenced, in particular at close proximity of the “hollow” nanoparticles but such type of nanostructure was not predominant (<15% of the total number of nanoparticles). For each of the first three nanostructures, the shell is essentially pure Pt (representative EEL spectra taken in the core or in the shell of the aged nanoparticles are provided in Fig. S2). Using the approach described in Ref. [20], we estimated that the Pt-shell thickened from 3.4 to 6.8 monolayers (0.76–1.50 nm) for the aged nanoparticles that retained a core-shell structure (Fig. 4c), and from 3.4 to almost 18.6 monolayers for the “hollow” nanoparticles (1.4–4.1 nm). Interestingly, the size of the “hollow” nanoparticles depends on the thickness of Pt-shell (Fig. 5). This result suggests that the increase in crystallite size caused by the electrochemical Ostwald ripening (dissolution of Pt-Co/C nanocrystallites, formation and redeposition of Pt^{2+} ions) in PEMFC stationary conditions is more pronounced in the zones of the catalytic layer where “hollow” nanoparticles are forming. To correlate the particle structure and composition, X-EDS analyses were also performed on individual nanoparticles: a progressive depletion in the average Co at% is observed from the fresh (19.0 ± 5 at%) to the “hollow” nanoparticles (4.1 ± 3 at%); an intermediate Co content being monitored for the core-shell nanoparticles (13.9 ± 13 at%). Typical X-EDS spectra measured on the different nanostructures are shown in Fig. S3.

The results obtained in this study irrefutably show that “hollow” nanoparticles form from pristine $\text{Pt}_3\text{Co/C}$ nanoparticles under real-life stationary PEMFC operating conditions, in agreement with our previous HAADF-STEM observations [14,40]. They also strikingly mark the difference with the results obtained from ASTs in potentiodynamic mode, for which core-shell nanoparticles composed of a thick Pt-shell covering the mother Pt-M alloy core are the unique morphology after electrochemical aging [13,18–20,25,37,41–43]. The results can be understood in view of the different partial pressure in oxygen used in each ageing test. Indeed, as explained in the introduction, ASTs are typically performed under inert atmosphere where Ostwald ripening and migration/aggregation are the predominant degradation mechanisms [25,28]. At variance, the large oxygen coverage that sets-up on the catalyst surface at high cathode potential (surface oxide formation from water splitting) and under O_2 atmosphere (note that air was used in this study) promotes different rearrangement of the catalyst nanostructure. There are numerous theoretical evidences from density functional theory calculations, *ab-initio* and classical molecular dynamics simulations [44–48] that, as the surface coverage by oxygen increases, the Co concentration in the surface layers of a Pt_3Co electrocatalyst increases, and the amount of Pt in the subsurface layers decreases. These atomistic simulations indicate that the greater oxophilicity of Co atoms does enable their segregation to the (sub)surface of the electrocatalyst. The Co atoms are not stable in the subsurface layers, but are rapidly dissolved in the acid electrolyte through the “place-exchange” of oxygen and platinum atoms. Using X-ray absorption spectroscopy, Kongkanand et al. [49] recently evidenced

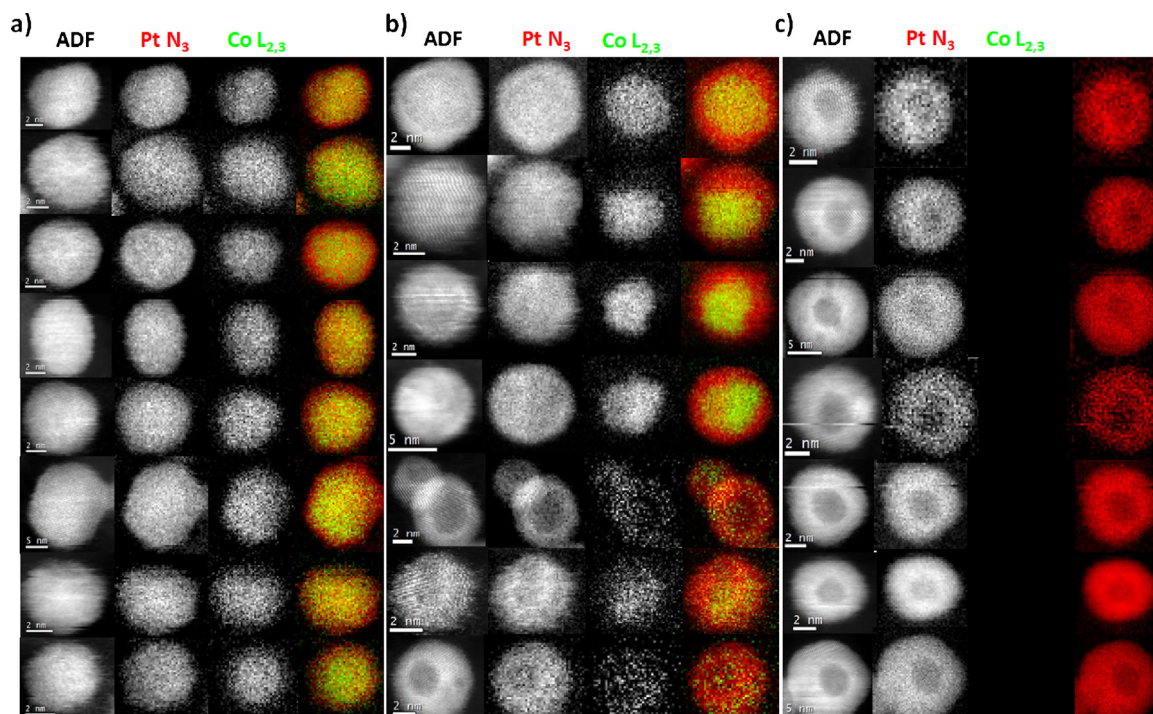


Fig. 4. Structural modification of Pt–Co/C nanoparticles aged in a PEMFC environment. ADF images and chemical maps of individual nanoparticles are displayed in (a) for the fresh catalyst and (b–c) for the aged one. The spectroscopic maps provide direct evidence of the core–shell nanostructure of the fresh Pt₃Co/C nanoparticles, resulting from acid-leaching and indicate that some aged nanoparticles maintain their core–shell nanostructure, while others display a “hollow” nanostructure. The Pt N₃ signal is shown in red, and the Co L_{2,3} signal is shown in green. (For interpretation of the references to color in this figure legend, the reader is referred to the web version of this article.)

that the “place-exchange” initiates above 1.10 V vs. RHE in O₂-free atmosphere, and above 0.75 V vs. RHE in the presence of O₂ in the electrolyte. Consequently, it is not surprising that the loss in Co is more pronounced under PEMFC operating conditions than in AST (see Fig. S4 for the variation of the averaged cell voltage during the PEMFC test). To balance the fast flux of Co atoms diffusing to the surface, an opposing flow of vacancies enters the material and aggregate in the centre of the nanoparticle thereby yielding “hollow” nanostructures (nanoscale Kirkendall effect) [14,19,50–54].

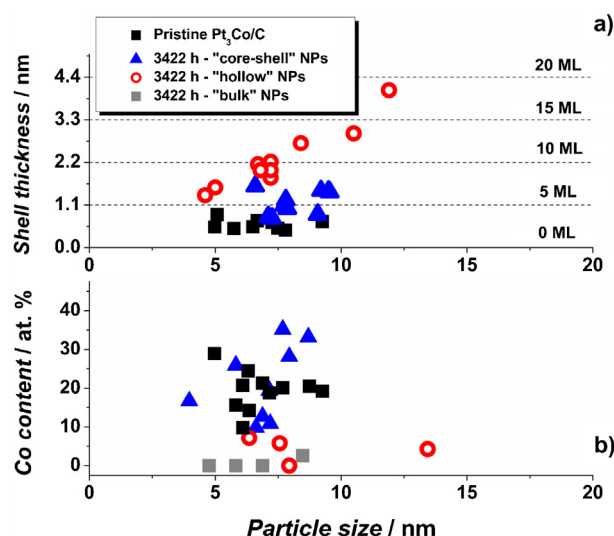


Fig. 5. Structure–chemical composition of the fresh and aged Pt–Co/C nanoparticles. (a) Histogram of the Pt-shell thickness and (b) chemical composition measured by X-EDS on the fresh (square), aged “core-shell” (triangles) and aged “hollow” (open circles) nanostructures, represented as a function of the nanoparticle size.

It is also striking that the zones of the aged cathode where “hollow” nanoparticles are detected feature (i) lower density of isolated nanoparticles, (ii) larger particle size and degree of agglomeration and (iii) lower Co content (Fig. 6b). Such features are typical of migration/agglomeration, electrochemical Ostwald ripening, and Co dissolution processes: their occurrence suggests that these zones were practically operative (effective), i.e. both electronically and ionically-connected, and accessible to oxygen during PEMFC operation. On the contrary, other regions of the aged catalytic layer are essentially characterized by well-distributed Pt–Co/C nanoparticles with Co atomic fraction close to that of the fresh material (Fig. 6a and c), likely due to insufficient access of oxygen and/or to the lack of electronic/ionic percolation. A rough estimation by HAADF–STEM indicates that *ca.* 20% of the metal nanoparticles possess a “hollow” nanostructure. Such value is close to that observed in our previous study (17%) [40], and to the fraction of utilized catalyst estimated by Lee et al. during PEMFC operation (15%), [55,56] thereby strongly supporting this assumption.

We now focus on the changes in surface reactivity and catalytic activity of the Pt–Co/C nanoparticles over time. Fig. 7 shows the base and the CO_{ad} stripping voltammograms measured on the fresh and the aged Pt–Co/C nanocatalysts. Large changes are observed in the potential region where underpotential hydrogen (H_{upd}) is adsorbed and desorbed (0.05 < E < 0.40 V vs. RHE). In particular, the H_{upd} region is almost featureless on the fresh Pt₃Co/C electrocatalyst, but adopts increased Pt-character over time (development of sharp current peaks). These results nicely parallel our EELS–SI observations that the Pt-shell thickens for both core–shell and “hollow” nanoparticles during PEMFC operation. Above 0.70 V vs. RHE, the relevant potential region for the PEMFC cathode, the increasing charge density of the surface oxide reduction peak indicate stronger Pt–oxygen bond strength on the aged Pt–Co/C surface [12,57]. In CO_{ad} stripping voltammograms, the development of a current

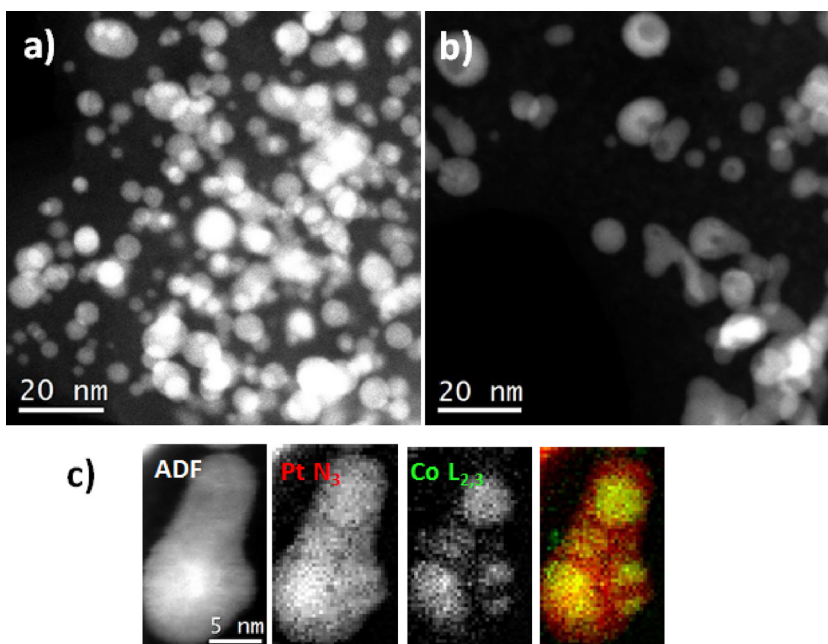


Fig. 6. Representative HAADF-STEM images of regions of the aged catalytic layer where (a) core-shell and (b) "hollow" nanostructures are found, (c) typical EELS elemental map of a sintered Pt-Co/C nanoparticle.

pre-peak at potential more negative than that of the main peak and the higher symmetry of the main peak point towards increasing fraction of aggregated metal nanoparticles and larger crystallite sizes for the aged nanocrystallites, respectively [12,58,59].

Summing up, the electrochemical observations confirm an increase of the mean Pt-Co/C particle size and of the fraction of agglomerated nanoparticles, thereby remarkably paralleling the analyses derived from electron microscopy [12].

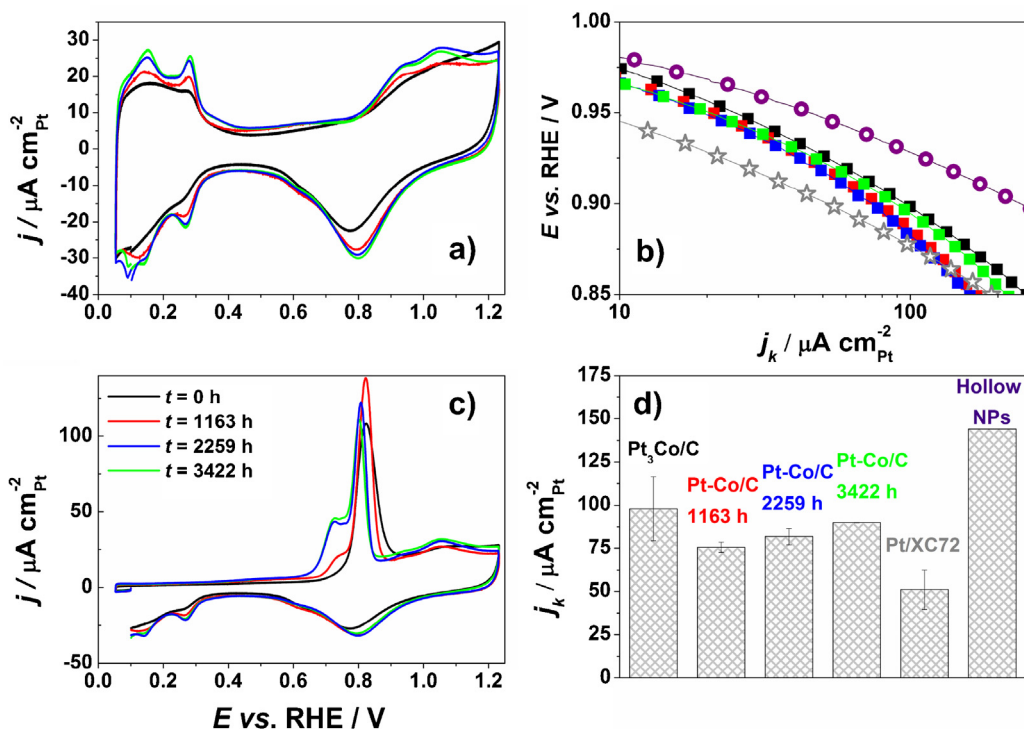


Fig. 7. Electrochemical studies performed on the Pt₃Co/C electrocatalyst in its native form or aged at constant current density ($j = 0.60 \text{ A cm}^{-2}$) at $T = 343 \text{ K}$ for different life stages and on the synthesized "hollow" Pt/C nanoparticles. (a) Base and (c) CO_{ad} stripping voltammograms of the fresh/aged Pt-Co/C catalysts. Electrolyte: 0.1 M H₂SO₄; $\nu = 0.020 \text{ V s}^{-1}$; $T = 298 \pm 1 \text{ K}$, no RDE rotation, catalysts loading $30 \mu\text{g Pt-Co/C}$ or $\mu\text{g Pt/C}$ geometrical cm^{-2} . The currents are normalized to the real surface area estimated from CO_{ad} stripping coulometry. Each voltammogram is the average of at least three measurements. (b) Tafel plots of the mass-transport corrected kinetic current obtained from the steady-state $I-E$ curves at $\omega = 1600 \text{ rpm}$, and (d) ORR specific activity evaluated at $E = 0.90 \text{ V}$ vs. RHE in O₂-saturated 0.1 M H₂SO₄; potential sweep rate 0.002 V s^{-1} ; positive-going potential sweep from 0.40 to 1.10 V vs. RHE; $T = 298 \pm 1 \text{ K}$. The currents are normalized to the real surface area estimated by CO_{ad} stripping coulometry. The pure Pt/C benchmark catalyst is a 40 wt% Pt/C purchased from E-TeK.

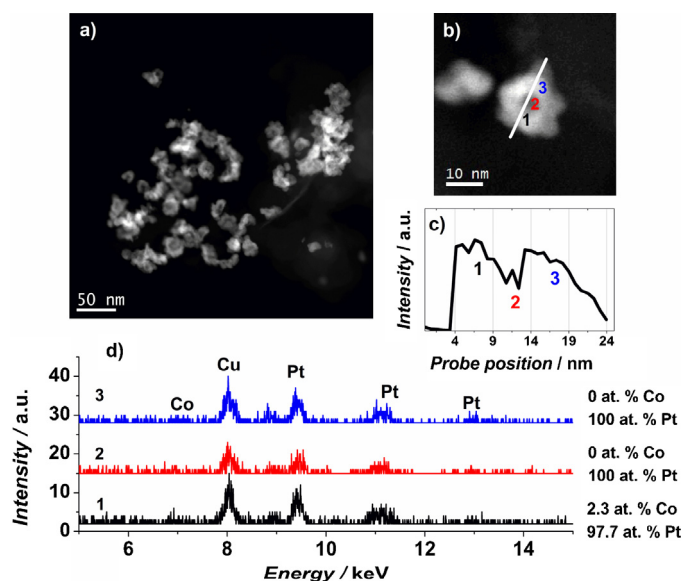


Fig. 8. Nanoanalytical characterization of the “hollow” Pt/C nanoparticles. (a) HAADF-STEM image of an individual “hollow” Pt/C nanoparticle, (b) zoom of a nanoparticle shown in (a). The bold line serves as a visual guide to indicate the location of the X-EDS line scan profile. (c) HAADF-STEM signal recorded at each point in the scan, (d) X-EDS spectra extracted from the sites marked as 1, 2 and 3.

The Tafel plots obtained from the steady-state I - E curves, and the ORR specific activities (SA) evaluated at $E = 0.90$ V vs. RHE for the fresh and the aged electrocatalysts are presented in Fig. 7b and d, respectively. A series of Koutecky–Levich plots is also provided in Fig. S5. Interestingly, the ORR specific activity is depreciated during the first 1163 h of operation, and increases over the last 2300 h. Such catalytic trend suggests that negative and positive catalytic effects compete to determine the final value of SA. The negative effects include the loss in Co from the fresh catalytic material, the thicker Pt-shell and the release of Co^{2+} ions in the ionomer/proton exchange membrane [12,13,26]. As shown in our previous studies, [12,60] the loss of Co atoms from the pristine $\text{Pt}_3\text{Co}/\text{C}$ nanocrystallites increases the coverage by oxygenated species (OH_{ad} and ORR intermediates), thereby strongly limiting the adsorption and dissociation of O_2 molecules and yielding smaller values of SA [12]. Moreover, the release of Co^{2+} ions inside the ionomer/PEM poisons the sulfonic acid groups of Nafion®, hinders their O_2 transport properties and lowers the intrinsic ORR activity of the metal nanoparticles [61].

On the positive side, the formation of “hollow” nanoparticles is necessarily beneficial to the electrocatalytic activity of the PEMFC cathode, in agreement with what was proposed by Dubau et al. [14] and Wang et al. [53]. Indeed, since these nanoparticles are nearly depleted in Co ($\text{Co} \leq 5$ at%, see Fig. S3), they cannot release significant amount of Co^{2+} ions in the catalytic layer. Moreover, their “hollow” nanostructure modifies the electronic and structural properties of Pt. In a recent theoretical study, Callejas-Tovar et al. [62] suggested that subsurface vacancies contract the lattice parameter of Pt surface atoms, and induce weaker binding energies of oxygenated species, which may partially account for the enhancement in ORR activity of the aged catalytic layer. Finally, as observed from HAADF and STEM-EELS measurements, the “hollow” nanoparticles possess larger particle size and lower concentration of low coordination sites (spherical shape) that strongly bind OH_{ad} groups: these effects also play a positive role on the ORR kinetics [53,63].

To further support our hypotheses, “hollow” metal nanoparticles were synthesized in-house following the experimental procedure described in Ref. [33], and characterized in liquid

electrolyte (Fig. S6). In the used synthesis procedure, the formation of “hollow” nanostructures is governed by the nanoscale Kirkendall effect and the galvanic replacement of Co atoms by Pt atoms (see Section 2). An additional acid leaching for 24 h in 0.1 M H_2SO_4 at room temperature ensured the removal of excess Co atoms (that is the Co atoms that were not covered by Pt atoms). Fig. 8 shows a representative HAADF-STEM image, and the associated X-EDS profile analysis of the obtained catalyst: the metal nanoparticles feature irregular shape, and sizes varying between 10 and 20 nm, which are structurally similar to the “hollow” nanostructures forming in real MEAs; these nanoparticles are compact, contain little (*ca.* 2–5 at%) or no Co atoms inside their lattice and feature a closed cavity in their centre. It is remarkable that their ORR activity is 1.5-fold that of the pristine $\text{Pt}_3\text{Co}/\text{C}$ and 3-fold that of state-of-the-art Pt/C nanoparticles (Fig. 7) with similar crystallite size, thereby validating the above-mentioned scenario, and offering a new route to the synthesis of highly active PEMFC electrocatalysts.

4. Conclusions

In this study, we reported with atomic detail the changes in structure and composition of Pt–Co/C nanocrystallites during a long-term PEMFC aging test (3422 h). The experimental results show that four different nanostructures are forming under the harsh cathode conditions: Pt, Pt–Co/C “hollow”, Pt–Co core-shell and Pt “bulk” nanoparticles. The formation of the “hollow” nanoparticles is attributed to the tendency of cobalt atoms to segregate to the surface under large coverage of oxygen and at PEMFC operating temperature. Therefore, their presence in some regions of the catalytic layer signs full effectiveness of these zones. Using positively the nanoscale Kirkendall effect, we synthesized in-house “hollow” nanoparticles, which are structurally similar to the “hollow” nanostructures forming in real membrane assemblies. Due to their larger crystallite size, their spherical shape and the presence of subsurface vacancies, their ORR specific activity is 1.5-fold that of the fresh $\text{Pt}_3\text{Co}/\text{C}$ cathode catalyst and 3-fold that of Pt/C nanocrystallites of the same size. Last but not least, our results raise important questions on the reliability of ASTs, which are currently used to determine the robustness of bimetallic cathode electrocatalysts. Indeed, during real-life PEMFC tests in stationary conditions, the bimetallic nanomaterial is exposed to small perturbations of the electrochemical potential but oxygen atmosphere: the presence of ORR intermediates at the surface, and even in the subsurface, act as a driving force for the surface segregation of the less noble element (Co) thereby yielding the formation of “hollow” nanoparticles. A contrario, since ASTs are usually performed under neutral atmosphere (Ar , N_2), they probably do not reflect the oxidizing atmosphere of a PEMFC cathode, and hence cannot correctly provide the changes of the chemical composition and of the fine nanostructure of Pt-based bimetallic nanoparticles.

Acknowledgements

The authors acknowledge financial support by Oseo-All through the H2E project. M.L.H. thanks the MECD Spanish Ministry (ref. EX2010-1135) for funding his post-doctoral stay at CEA-Grenoble. M.C. thanks the French University Institute (IUF) for its support.

Appendix A. Supplementary data

Supplementary data associated with this article can be found, in the online version, at <http://dx.doi.org/10.1016/j.apcatb.2014.01.034>.

References

- [1] M. Watanabe, K. Tsurumi, T. Mizukami, T. Nakamura, P. Stonehart, J. Electrochem. Soc. 141 (1994) 2659–2668.
- [2] T. Toda, H. Igarashi, H. Uchida, M. Watanabe, J. Electrochem. Soc. 146 (1999) 3750–3756.
- [3] V.R. Stamenkovic, B.S. Mun, K.J.J. Mayrhofer, P.N. Ross, N.M. Markovic, J. Am. Chem. Soc. 128 (2006) 8813–8819.
- [4] V.R. Stamenkovic, B. Fowler, B.S. Mun, G.F. Wang, P.N. Ross, C.A. Lucas, N.M. Markovic, Science 315 (2007) 493–497.
- [5] J. Greeley, I.E.L. Stephens, A.S. Bondarenko, T.P. Johansson, H.A. Hansen, T.F. Jaramillo, J. Rossmeisl, I. Chorkendorff, J.K. Nørskov, Nat. Chem. 1 (2009) 552–556.
- [6] L. Gan, M. Heggen, S. Rudi, P. Strasser, Nano Lett. 12 (2012) 5423–5430.
- [7] I.E.L. Stephens, A.S. Bondarenko, U. Grønberg, J. Rossmeisl, I. Chorkendorff, Energy Environ. Sci. 5 (2012) 6744–6762.
- [8] C. Cui, L. Gan, M. Heggen, S. Rudi, P. Strasser, Nat. Mater. 12 (2013) 765–771.
- [9] L. Gan, M. Heggen, R. O'Malley, B. Theobald, P. Strasser, Nano Lett. 13 (2013) 1131–1138.
- [10] P. Yu, M. Pemberton, P. Plasse, J. Power Sources 144 (2005) 11–20.
- [11] H.R. Colon-Mercado, B.N. Popov, J. Power Sources 155 (2006) 253–263.
- [12] L. Dubau, F. Maillard, M. Chatenet, J. André, E. Rossinot, Electrochim. Acta 56 (2010) 776–783.
- [13] S. Chen, H.A. Gasteiger, K. Hayakawa, T. Tada, Y. Shao-Horn, J. Electrochem. Soc. 157 (2010) A82–A97.
- [14] L. Dubau, F. Maillard, M. Chatenet, L. Guétaz, J. André, E. Rossinot, Electrochim. Acta 56 (2011) 10658–10667.
- [15] S.C. Zignani, E. Antolini, E.R. Gonzalez, J. Power Sources 182 (2008) 83–90.
- [16] C.F. Yu, S. Koh, J.E. Leisch, M.F. Toney, P. Strasser, Faraday Discuss. 140 (2008) 283–296.
- [17] L. Dubau, F. Maillard, M. Chatenet, L. Guétaz, J. André, E. Rossinot, J. Electrochem. Soc. 157 (2010) B1887–B1895.
- [18] C.E. Carlton, S. Chen, P.J. Ferreira, L.F. Allard, Y. Shao-Horn, J. Phys. Chem. Lett. 3 (2012) 161–166.
- [19] M. Heggen, M. Oezaslan, L. Houben, P. Strasser, J. Phys. Chem. C 116 (2012) 19073–19083.
- [20] H.L. Xin, J.A. Mundy, Z. Liu, R. Cabezas, R. Hovden, L.F. Kourkoutis, J. Zhang, N.P. Subramanian, R. Makharia, F.T. Wagner, D.A. Muller, Nano Lett. 12 (2012) 490–497.
- [21] Z. Yu, J. Zhang, Z. Liu, J.M. Ziegelbauer, H. Xin, I. Dutta, D.A. Muller, F.T. Wagner, J. Phys. Chem. C 116 (2012) 19877–19885.
- [22] Q.Y. Jia, D.E. Ramaker, J.M. Ziegelbauer, N. Ramaswamy, A. Halder, S. Mukerjee, J. Phys. Chem. C 117 (2013) 4585–4596.
- [23] A. Ohma, K. Shinohara, A. Iiyama, T. Yoshida, A. Daimaru, ECS Trans. 41 (2011) 775–784.
- [24] F.R. Nikkuni, E.A. Ticianelli, L. Dubau, M. Chatenet, Electroanalysis 4 (2013) 104–116.
- [25] Y.C. Yu, H.L.L. Xin, R. Hovden, D.L. Wang, E.D. Rus, J.A. Mundy, D.A. Muller, H.D. Abruna, Nano Lett. 12 (2012) 4417–4423.
- [26] F. Maillard, L. Dubau, J. Durst, M. Chatenet, J. André, E. Rossinot, Electrochem. Commun. 12 (2010) 1161–1164.
- [27] L. Dubau, J. Durst, F. Maillard, M. Chatenet, L. Guétaz, J. André, E. Rossinot, Fuel Cells 12 (2012) 188–198.
- [28] L. Dubau, L. Castanheira, G. Berthomé, F. Maillard, Electrochim. Acta 110 (2013) 273–281.
- [29] Z. Zhao, L. Dubau, F. Maillard, J. Power Sources 217 (2012) 449–458.
- [30] C.C. Herrmann, G.G. Perrault, A.A. Pilla, Anal. Chem. 40 (1968) 1173–1174.
- [31] S. Bernal, F.J. Botana, J.J. Calvino, C. López-Cartes, J.A. Pérez-Omil, J.M. Rodríguez-Izquierdo, Ultramicroscopy 72 (1998) 135–164.
- [32] E.J. Kirkland, Advanced Computing in Electron Microscopy, second ed., Springer, 2010.
- [33] S.J. Bae, S.J. Yoo, Y. Lim, S. Kim, Y. Lim, J. Choi, K.S. Nahm, S.J. Hwang, T.H. Lim, S.K. Kim, P. Kim, J. Mater. Chem. 22 (2012) 8820.
- [34] H. Schulenburg, E. Muller, G. Khelashvili, T. Roser, H. Bonnemann, A. Wokaun, G.G. Scherer, J. Phys. Chem. C 113 (2009) 4069–4077.
- [35] H. Schulenburg, J. Durst, E. Müller, A. Wokaun, G.G. Scherer, J. Electroanal. Chem. 642 (2010) 52–60.
- [36] M. Uchida, Y.C. Park, K. Kakinuma, H. Yano, D.A. Tryk, T. Kamino, H. Uchida, M. Watanabe, Phys. Chem. Chem. Phys. 15 (2013) 11236–11247.
- [37] B. Patrick, H.C. Ham, Y. Shao-Horn, L.F. Allard, G.S. Hwang, P.J. Ferreira, Chem. Mater. 25 (2013) 530–535.
- [38] F. de la Peña, M.H. Berger, J.F. Hocheplid, F. Dynys, O. Stephan, M. Walls, Ultramicroscopy 111 (2011) 169–176.
- [39] S. Trasobares, M. Lopez-Haro, M. Kociak, K. March, F. de la Peña, J.A. Pérez-Omil, J.J. Calvino, N.R. Lugg, A.J. D'Alfonso, L.J. Allen, C. Colliex, Angew. Chem. Int. Ed. 50 (2011) 868–872.
- [40] L. Dubau, J. Durst, L. Guétaz, F. Maillard, M. Chatenet, J. André, E. Rossinot, ECS Electrochem. Lett. 1 (2012) F13–F15.
- [41] K.C. Neyerlin, R. Srivastava, C. Yu, P. Strasser, J. Power Sources 186 (2009) 261–267.
- [42] M. Oezaslan, M. Heggen, P. Strasser, J. Am. Chem. Soc. 134 (2011) 514–524.
- [43] F. Hasché, M. Oezaslan, P. Strasser, J. Electrochem. Soc. 159 (2012) B25–B34.
- [44] Y. Ma, P.B. Balbuena, J. Chem. Theory Comput. 4 (2008) 1991–1995.
- [45] Y.D. Yin, R.M. Rioux, C.K. Erdonmez, S. Hughes, G.A. Somorjai, A.P. Alivisatos, Science 304 (2004) 711–714.
- [46] R. Callejas-Tovar, P.B. Balbuena, Phys. Chem. Chem. Phys. 13 (2011) 20461–20470.
- [47] R. Callejas-Tovar, W. Liao, H. Mera, P.B. Balbuena, J. Phys. Chem. C 115 (2011) 23768–23777.
- [48] P.B. Balbuena, R. Callejas-Tovar, P. Hirunsit, J.M. Martínez De La Hoz, Y. Ma, G.E. Ramírez-Caballero, Topics Catal. 55 (2012) 322–325.
- [49] A. Kongkanand, J.M. Ziegelbauer, J. Phys. Chem. C 116 (2012) 3684–3693.
- [50] A.D. Smigelskas, E.O. Kirkendall, Trans. AIME 171 (1947) 130–142.
- [51] Y.D. Yin, R.M. Rioux, C.K. Erdonmez, S. Hughes, G.A. Somorjai, A.P. Alivisatos, Science 304 (2004) 711–714.
- [52] R. Callejas-Tovar, C.A. Diaz, J.M.M. de la Hoz, P.B. Balbuena, Electrochim. Acta 101 (2013) 326–333.
- [53] J.X. Wang, C. Ma, Y. Choi, D. Su, Y. Zhu, P. Liu, R. Si, M.B. Vukmirovic, Y. Zhang, R.R. Adzic, J. Am. Chem. Soc. 133 (2011) 13551–13557.
- [54] Y. Zhang, C. Ma, Y.M. Zhu, R. Si, Y. Cai, J.X. Wang, R.R. Adzic, Catal. Today 202 (2013) 50–54.
- [55] M. Lee, M. Uchida, H. Yano, D.A. Tryk, H. Uchida, M. Watanabe, Electrochim. Acta 55 (2010) 8504–8512.
- [56] M. Lee, M. Uchida, D.A. Tryk, H. Uchida, M. Watanabe, Electrochim. Acta 56 (2011) 4783–4790.
- [57] S. Mukerjee, J. McBreen, J. Electroanal. Chem. 448 (1998) 163–171.
- [58] F. Maillard, S. Schreier, M. Hanzlik, E.R. Savinova, S. Weinkauff, U. Stimming, Phys. Chem. Chem. Phys. 7 (2005) 385–393.
- [59] F. Maillard, E.R. Savinova, U. Stimming, J. Electroanal. Chem. 599 (2007) 221–232.
- [60] L. Dubau, M. Lopez-Haro, L. Castanheira, J. Durst, M. Chatenet, P. Bayle-Guillemaud, L. Guétaz, N. Caqué, E. Rossinot, F. Maillard, Appl. Catal., B 142–143 (2013) 801–808.
- [61] J. Durst, M. Chatenet, F. Maillard, Phys. Chem. Chem. Phys. 14 (2012) 13000–13009.
- [62] R. Callejas-Tovar, P.B. Balbuena, J. Phys. Chem. C 116 (2012) 14414–14422.
- [63] Y. Cai, C. Ma, Y. Zhu, J.X. Wang, R.R. Adzic, Langmuir 27 (2011) 8540–8547.